

## Optimal bioelectric control accelerates collective wound healing

Jeremy S. Yodh<sup>1,2,†,§</sup>, Yubin Lin<sup>3,†</sup>, Sumit Sinha<sup>4,‡</sup>, Vishaal Krishnan<sup>4,‡</sup>, L. Mahadevan<sup>4,5,§</sup>, and Daniel J. Cohen<sup>1,2,§</sup>

<sup>1</sup>Department of Mechanical and Aerospace Engineering, Princeton University, Princeton, NJ, 08540, USA

<sup>2</sup>Omenn-Darling Bioengineering Institute, Princeton University, Princeton, NJ, 08540, USA

<sup>3</sup>Department of Electrical and Computer Engineering, Princeton University, Princeton, NJ, 08540, USA

<sup>4</sup>School of Engineering and Applied Sciences, Harvard University, Cambridge, MA 02138, USA

<sup>5</sup>Departments of Physics and Organismic and Evolutionary Biology, Harvard University, Cambridge, MA 02138, USA

<sup>†</sup>These authors contributed equally; <sup>‡</sup>These authors contributed equally

<sup>§</sup>Corresponding authors: jy1522@princeton.edu (J.S.Y.), lmahadev@g.harvard.edu (L.M.), and danielcohen@princeton.edu (D.J.C.)

### Abstract

Effective wound healing relies on thousands of cells collectively migrating to close the gap. It is increasingly clear that part of this migration is driven by endogenous electrochemical fields which point towards the center of skin wounds and guide collective cell migration through “electrotaxis”. Mounting evidence suggests exogenously applied electric fields can accelerate healing, but progress in this field has been limited by the use of brute-force, global stimulation strategies that are wound agnostic and reflect neither the collective nature of the healing process nor the dynamic nature of the wound geometry. Here, we develop an experimental system to study how monolayer mouse skin responds to spatiotemporally patterned electric fields. We first show that local electrical stimulation can produce near global cell migration responses arising from cell-cell mechanical adhesion. We apply this strategy to 2D circular wounds using a local ring electric field near the wound edge and reveal how to tune the timing of local stimulation to avoid cellular jamming. Finally, we integrate our findings with a biophysics-informed optimal control strategy to tune both when and where the electric field should be applied in time, resulting in dramatic improvements to healing.

### Introduction

Healing even a small skin injury involves the coordinated behavior of thousands of cells to seal the wound<sup>1–3</sup>. Here, cells at the wound boundary must migrate and lead follower cells into the breach, while cells farther from the edge must balance division and migration. Self-healing emerges as a remarkable collective behavior from the local interactions of the constituent cells, and the collective cellular motion shares many similarities to other biological collectives such as bird flocks<sup>4–6</sup>, herds of sheep<sup>7–9</sup>, and human gatherings<sup>10–12</sup>. However, while we can heal, it is a slow process that is further delayed by disease and age<sup>13,14</sup>, and raises a natural question: how can it be accelerated?

A natural approach is to direct and promote collective cell migration. While numerous control techniques have emerged (e.g., optogenetic<sup>15–17</sup> and chemotactic<sup>18,19</sup>), electrotaxis or galvanotaxis—using electric fields to steer the directed migration of cells—is particularly apt because of its tunability<sup>20–31</sup>. This modality is conserved across most multicellular organisms<sup>32,33</sup> and arises independently from the nervous system. Animal skin cells, for example, transport negative ions outwards and positive ions inwards, maintaining a static transepidermal potential difference of ~50 mV<sup>32,34</sup>. Skin injuries, such as a laceration or burn, locally disrupt this potential landscape and lead to an ionic imbalance where the wound margin is more positively charged relative to the wound center resulting in a direct current (DC) flow and associated electric field of strengths ~1 V/cm. It is this field that many cells use to set both their migratory direction and speed in electrotaxis<sup>35,36</sup>. Controlling these ionic currents should allow us to direct cell migration during healing using an electric bandage.

However, while the wound currents *in vivo* have a stable spatial gradient that peaks near the wound margin and decays into the wound bed<sup>37,38</sup>, all extant bioelectric bandages that show (modest) healing improvements in animal models<sup>38–40</sup> rely on overpowering, global electric fields applied without respect to the size and shape of the wound itself. In fact, *in vitro* studies on mature skin cell sheets have shown that such global fields can cause mechanical damage<sup>20</sup> that result from trying to override the existing intrinsic collective dynamics across the tissue. In sharp contrast, many biological collective systems use local feedback-driven control strategies which minimize input costs to the controller and maximize the response of the collective<sup>41–44</sup>. Inspired by shepherding, where the shepherd nudges the herd and measures its local and global response, and then iteratively updates these nudges to steer the herd<sup>45–47</sup>, we hypothesized that local control has the potential to better synergize with the native collective dynamics in a group of cells. Here, we design and test these control strategies within the context of an electrotactic model wound system and show that they significantly outperform naïve control methods.

Our approach addresses this by answering three related questions: First, how does the migratory behavior of a tissue respond to a local electric input? Second, can we use this local electric stimulation to accelerate wound healing in a 2D wound model while maintaining tissue integrity? Third, can we start to optimally heal a wound? We investigate the first question by delivering local electric fields to the central zone of a quasi-1D tissue and observing the migratory response, comparing it to the response of traditional global electric stimuli<sup>20–25</sup>. Next, we show that a single pulse of a local, annular shaped electric field can improve healing rates substantially while avoiding common pitfalls of global control, e.g., tissue edge retraction and cell death<sup>20</sup>. Finally, we design a simple biophysically informed optimal control model embedded within the framework of stochastic optimal control. A minimal model leads to the prediction that a pulse train which follows the wound edge. When the model is subjected to experimental constraints, it predicts a two pulsed strategy where the pulses are spaced out in spacetime. We demonstrate this simple double pulse sequence further improves healing rates while

maintaining tissue integrity. Together, these observations provide evidence for how a combination of experimental observations and biophysical theory embedded within an optimal control framework allows us to accomplish more efficient wound healing strategies using localized spatial and temporal commands.

## Results

### Applying local electric cues to tissues and quantifying collective responses

We start by establishing a reproducible experimental system that can apply precise local electrical cues to tissues and then analyze the resulting collective dynamics to measure if local stimulation produces broader collective responses. We use engineered skin sheets both to emphasize the potential for controlling healing, and because the collective behavior of skin cells can be tuned by using calcium to alter cell-cell adhesion<sup>20,48,49</sup>. We grow reproducible 10 mm x 1.5 mm skin cell sheets by seeding cells into micro-stencils within the stimulation wells of a 24-well plate (Fig. 1A). After cells adhered in standard growth media, we elevate the calcium levels (from 50  $\mu\text{M}$  to 300  $\mu\text{M}$ ) to activate cell-cell adhesion and collectivity. Prior to imaging, we remove the stencil and stain the tissues with cytoplasmic and nuclear vital dyes. Full details can be found in the Supporting Information (SI section A).

To apply local electrical cues to living tissues, we adapt our SCHEPHERD system<sup>25</sup>—an 8-channel bioelectric stimulation platform designed for 24-well plates and validated for electrotaxis. Briefly, SCHEPHERD uses 3D-printed inserts, salt-bridge electrochemistry, and custom electronics to deliver physiological DC electric fields to tissues (see SI section A). We modify the inserts to contain a single, 340  $\mu\text{m}$  ridge (limited by the 3D printer), positioned just above the center of an engineered tissue (as in Fig. 1B). By forcing the applied current to travel through the constriction, we amplify the local electric field to produce a therapeutic current density only in the vicinity of the ridge over the tissue center. Ohm's law,  $E = J/\sigma$ , where  $E$  is the strength of the electric field,  $J$  is the current density, and  $\sigma$  is the conductivity of the medium provides the relationship between current density and electric field.

We next validate that the applied electric field was both sufficiently local and strong enough to generate a local electrotactic response. Since the current density from our ridged ceiling structure is near zero in the  $y$ -direction, it is characterized by its  $x$ -component,  $J_x$ , alone. To measure  $J_x$ , we inject 2  $\mu\text{m}$  diameter, charged, fluorescent beads into our bioreactor and apply a known voltage drop across the system. The local current density causes the charged beads to flow via electrophoresis which we measure using particle image velocimetry (PIV)<sup>50</sup> taking care to subtract the background convective flows. Equating the Stokes drag on the particle with the force from the electric

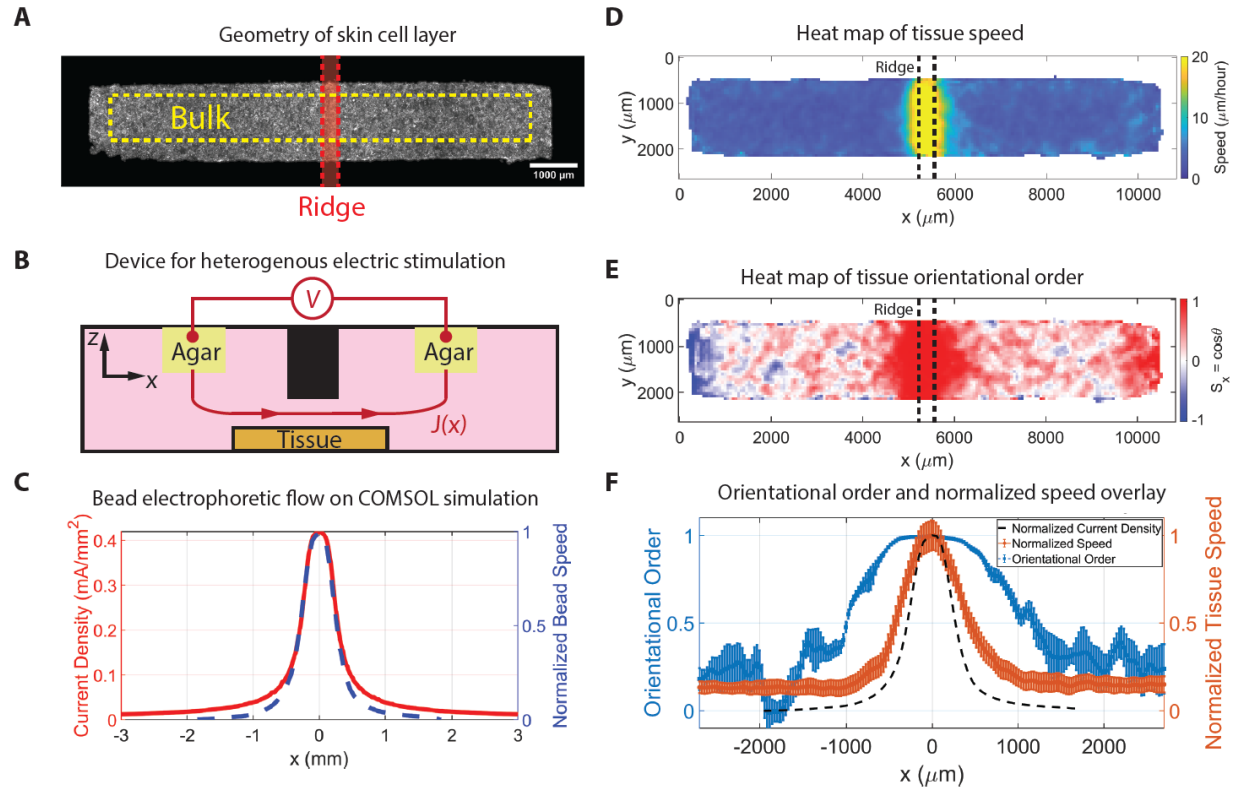


**Figure 1. Localized current density selectively drives collective migration.** (A) Micrograph of a quasi-1D tissue strip (10 mm x 1.5 mm) of primary mouse keratinocytes. The bulk of the tissue and zone with high current density are labeled. (B) Device schematic of 3D printed bioreactor set-up. A voltage difference is maintained across two agarose salt bridges which drives an ionic current across a tissue. The central ridge geometry concentrates the ionic current above the center of the tissue. (C) COMSOL simulation of the current density in the  $x$ -direction (red) showing strongly localized current density. Overlaid (blue dashed line) is the normalized  $x$ -component of the velocity of charged beads flowing in ridge device showing that the COMSOL simulation accurately scales with the ground truth. (D-E) Heat maps of the average tissue speed and the average  $x$ -component of the orientational order,  $S_x$ , averaged over the middle hour of stimulation which show the localized migratory response of the tissue averaged over  $N \geq 6$  samples. (F) Unit normalized speed (orange, right axis) and orientational order (blue, left axis) plotted spatially with the ridge center at  $x = 0$ . Data is the average response from the middle hour of experiment. The unit normalized current density derived from the COMSOL simulation is plotted as a dashed black line.

field is sufficient to show that the  $x$ -component of the velocity of the charged beads,  $v_x$ , scales with  $J_x$  and the electric field. To provide an absolute scale for the current density, we perform COMSOL simulations of our system. Fig. 1C shows the normalized  $v_x$  overlaid on the current density results from the COMSOL simulation, and indicates an effective electrical stimulation zone of  $\sim 1$  mm with a peak current density of  $J_x = 0.42$  mA/mm<sup>2</sup> (corresponding peak electric field strength of  $E \sim 2.5$  V/cm). This field is larger than, but comparable to, endogenous electric fields in the body.

Knowing the approximate spatial footprint of the stimulation zone, we set an appropriate length scale for an engineered tissue to ensure both that our stimulation zone was small relative to the tissue length ( $\sim 1/10^{\text{th}}$  the tissue length), and that we can ignore edge effects far to the right and left of the stimulation zone. We therefore grow 10 mm x 1.5 mm skin monolayer patches using primary mouse skin cells and expose tissues to the following electrical stimulation structure: thirty minutes of control ( $E = 0$ ), three hours of electrical

stimulation with a peak field strength of  $E = 2.5$  V/cm, and four and a half hours of relaxation ( $E = 0$ ). Full experimental methods are provided in the SI.

To measure the tissue-scale response, we perform PIV on fluorescent timelapse data of cell migration ( $N = 6$ ) to generate vector flow fields of the dynamics, which we highlight in Figs. 1D-E. First, we assess local migration speed (magnitude of the  $x$  and  $y$  velocity components summed), where we observe the expected increase in cell migration speed during electrotaxis<sup>22,25</sup> but only in the electrically stimulated region, with cells outside this region effectively unaware of the stimulus. Directionality or orientational order (Fig. 1E), shows a similar localized response emphasizing local, rightward migration of cells within the stimulated region. Here, we define directionality as  $S_x = \cos \theta$  where  $\theta$  is the angle between the applied electric field and the tissue velocity.  $S_x$  measures how aligned or anti-aligned the tissue motion is with the applied electrical stimuli;  $S_x = 1$  (red, rightwards) corresponds to perfect alignment and  $S_x = -1$  (blue, leftwards) corresponds to perfect anti-alignment. Raw timelapses and heatmap videos can be found in the Supplementary Video 1 and 2 respectively, and the divergence of the flow field (see Fig. S1) is discussed in the SI section B.

A key feature of controlling collectives is that even hyper-localized stimulus can result in long range collective responses as information and awareness of the stimulation spreads throughout the group. This spread of information is why in Figs. 1D and 1E, the speed is tightly coupled to the electrical input while the orientational order is significantly broadened. To capture this difference, we overlay the normalized speed and orientational order averaged over the middle hour of the stimulation period on the electrical input in Fig. 1F. Supporting data is provided in the SI section B: kymographs of speed and orientational order (Fig. S2), transfer functions for the speed and orientational order as a function of current density (Fig. S3), and analogue overlays of orientational order and input field shape for tissues of varying cell-cell coupling (Fig. S4) which demonstrates that increasing coupling causes the ordered zone to broaden. Using the full-width-half-max (FWHM) to quantify the spatial extent of the response, we find that directionality is affected over a region more than twice as large ( $\sim 2000$   $\mu\text{m}$ ) than that of speed ( $\sim 700$   $\mu\text{m}$ ). Nondimensionalizing these values by the FWHM of current density ( $\sim 550$   $\mu\text{m}$ ), provides an estimate of how tightly the responses are coupled to the input stimulus. While the nondimensionalized FWHM for speed is  $\sim 1.3$ , the nondimensionalized FWHM for order is  $\sim 3.6$ . One implication of this is that a small number of well-spaced, local stimuli can produce a spanning effect over the entire tissue. See SI section D and Fig. S5 for details.

### **Accelerating circular wound healing using a 2D ring stimulus**

Knowing the input-output response of a group and the length scales over which information flows for a given stimulus allows us to more precisely control the collective. Here, we demonstrate this concept by attempting to accelerate the healing of 2D, circular puncture wounds in our engineered tissues. For these experiments, we modify our 1D ridge into a 2D annular ring, and focus on wounds diameter  $d \in [0.5, 1]$  mm. A full protocol to create circular wounds can be found in the SI section A.

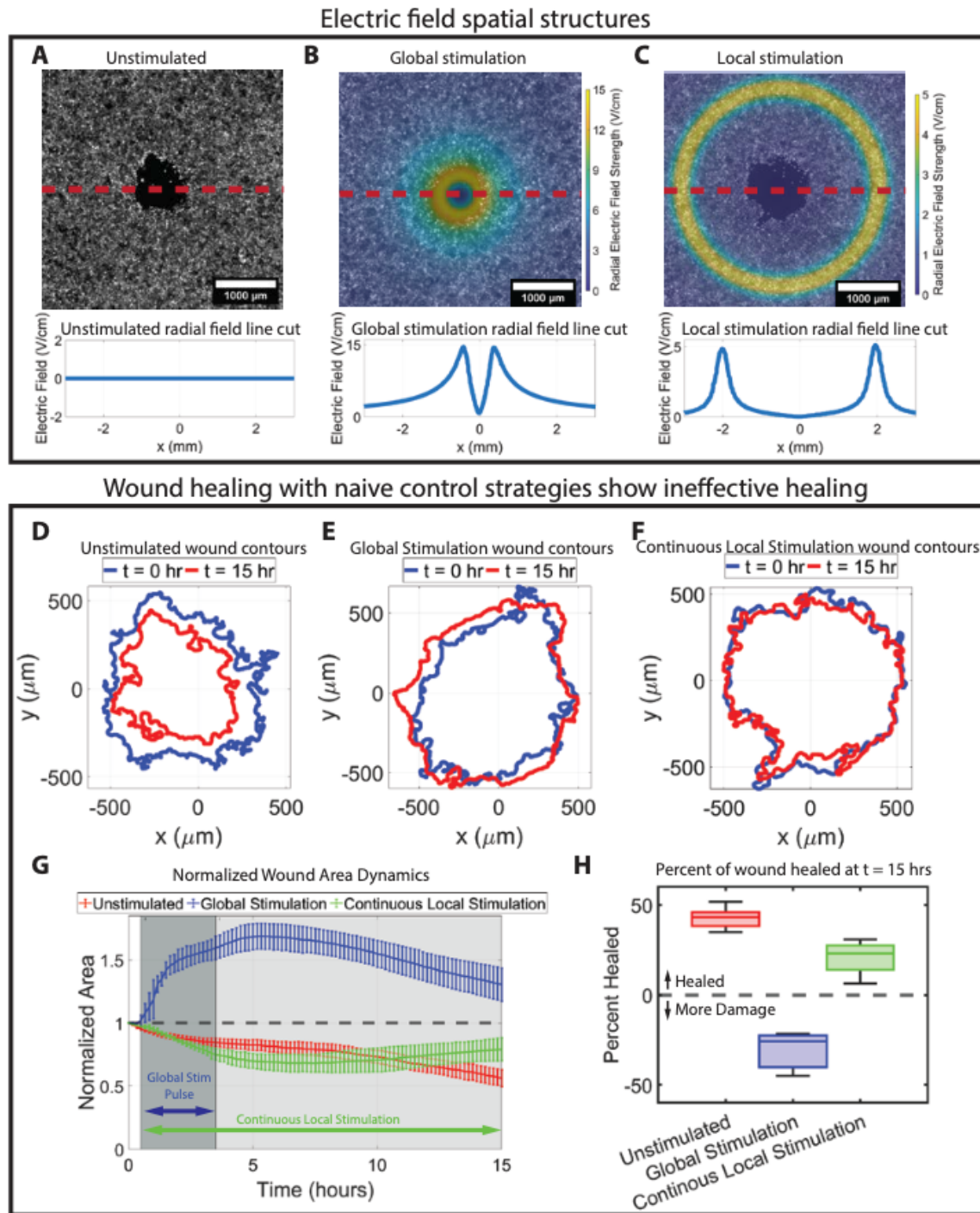


Figure 2. Stimulation structures in 2D applied without care show poor healing. (A-C) Spatial stimulation patterns overlaid on representative micrographs of wounded tissues at  $t = 0$  hrs with color corresponding to field strength (top) and radial field line cuts through the dashed-red centerline for (A) Unstimulated, (B) Global Stimulation with monopole-like electric field, and (C) Local Stimulation with a ring electric field. (D-F) Wound contours taken at the beginning  $t = 0$  hrs (blue), and the end,  $t = 15$  hrs (red), of representative experiments for (D) Unstimulated, (E) Global Stimulation, and (F) Continuous Local Stimulation, which uses the ring field continuous for the duration of the experiment. (g) Normalized wound area,  $A(t)$ , as a function of time for the various stimulation strategies. The horizontal dashed line at  $A(t) = 1$  corresponds to the initial area of the wound. The dark grey shaded region from  $t \in [0.5, 3.5]$  hrs is the time where stimulation for the Global Stimulation was on and the light grey shaded region between  $t \in [0.5, 15]$  hrs corresponds to when the Continuous Local Stimulation was on. (H) The percentage healed of each wound at  $t = 15$  hrs averaged over averaged over  $N \geq 3$  samples for the various stimulation strategies.

We first compare healing rates of the two limiting cases—unstimulated wounds (Fig. 2A and Supplementary Video 4) and wounds treated with “Global Stimulation” directing all cells to the wound center (Fig. 2B and Supplementary Video 5)—to the healing rates of wounds treated with the local ring stimulus (Fig. 2C). Figs. 2A-C also show 2D field strength heatmaps overlaid on micrographs of wounded tissues, along with their diametric profiles (below each image) of the applied electrical fields simulated in COMSOL.

Unstimulated wounds heal driven by baseline migration and proliferation driving the wound edge inwards and healing slowly (Fig. 2D and Supplementary Video 4). In contrast, the Global Stimulation cases, which use a monopole-like field results in immediate, radial edge retraction causing the wound to grow (Fig. 2E and see Supplementary Video 5; note red contour is bigger than blue). Edge retraction has been observed before and specifically arises from a global stimulus competing with the native collective behaviors within the tissue<sup>20</sup>. Hence, this naïve, Global Stimulation makes the wound worse.

We compare these baselines to our first attempt at local control using the ring stimulus (2C and Supplementary Video 6). Specifically, we place an annular ridge at  $R = 1.75$  mm from the wound center creating the ring-shaped field shown in the overlay and profile in Fig. 2C and apply continuous stimulation from  $t = 0.5$  hrs to  $t = 15$  hrs (labeled “Continuous Local Stimulation” in figures). We set this ridge radius such that the radial distance between the ridge and the wound edge was order  $\approx 1.0$  mm, a length scale informed by our 1D ridge experiments and 2D non-concentric stimulated wound healing assays (see SI section E, Fig. S6, and Supplementary Video 7). The ridge placement is critical: it must be far enough from the wound edge to avoid edge retraction, yet close enough to orient cell migration radially inwards to accelerate wound closure. While the resulting stimulus did not cause retraction or make the wound larger, it surprisingly results in slower healing when compared to the unstimulated case, as shown in Fig. 2F.

To understand why healing was slower, we examine the healing dynamics by plotting normalized area as a function of time, shown in Fig. 2G. A horizontal dashed line at  $A = 1$  marks the initial area for each condition. Beginning with the unstimulated case (red trace), we see a slow, but monotonic healing process reaching  $A \approx 0.6$  (40% healed) over the 15-hour experiment. By contrast, Global Stimulation (blue trace), immediately increases the wound area due to edge retraction and never recovers. Interestingly, the continuous local stimulation does produce faster initial healing than the unstimulated case (see Fig. S7 for separated plots of  $A(t)$  by stimulation condition and Fig. S8 for plots of  $dA/dt$ ), but plateaus after  $\sim 3$  hours of electrical stimulation before gradually worsening. This demonstrates an improvement over the Global Stimulation case but remains worse than the unstimulated case. The endpoint data at  $t = 15$  hrs is summarized in Fig. 2H. The key results from this first attempt were, surprisingly, that local stimulation does solve the edge retraction issue, but fails to accelerate overall wound closure.

Why does the Continuous Local Stimulation initially accelerate healing but later plateau, and can we extend the period of accelerated healing? To understand these dynamics, we recall that the tissue is essentially a massive, 2D crowd of thousands of individual cells. Global radial inwards stimulation causes cells are to converge on the wound center,

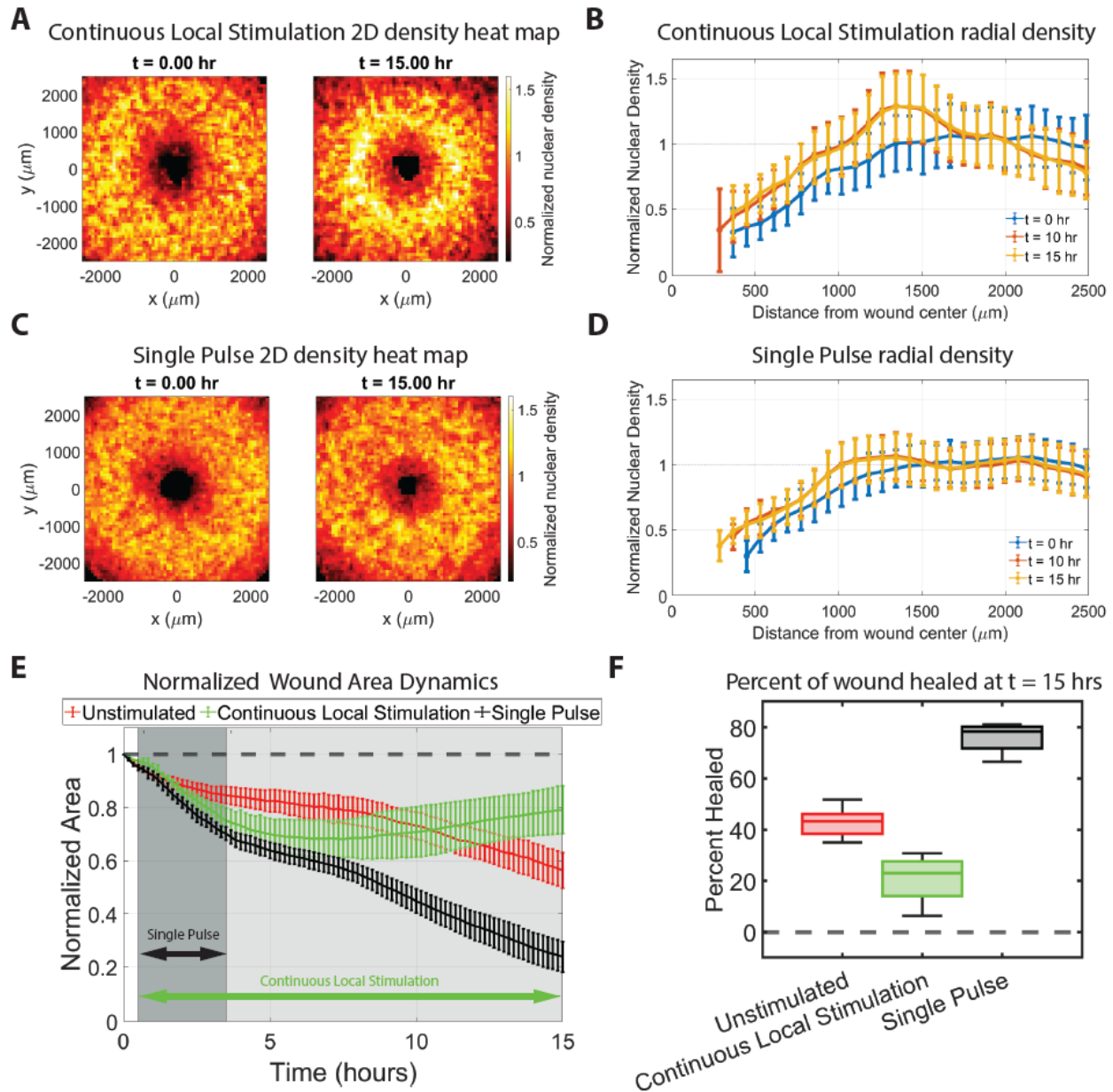


Figure 3. Single Pulse of local stimulation prevents density build-ups and allows for effective healing. (A) 2D average nuclear density heat maps from the Continuous Local Stimulation experiments at  $t = 0$  and  $t = 15$  hrs showing build-up of nuclear density from excessive stimulation. Color corresponds to local density. (B) Radial line profile of (A) at  $t = 0, 10, 15$  hrs showing build-up of density. (C) Same as (A) but for Single Pulse data. (D) Radial line profiles of (B) showing that density never grows large enough to induce a jam. (E) Normalized area dynamics for Continuous Local Stimulation (green), Single Pulse (black), and unstimulated (red) experiments with shaded regions and arrows denoting where the field was on for each case. (F) The percent healed of each wound at  $t = 15$  hrs averaged over  $N \geq 3$  samples for the two spatial local stimulation strategies shows improved healing for the pulsed samples with the unstimulated case shown for comparison.

eventually crowding against their neighbors and locking into place in a radial traffic jam (an analogue to the load-supporting arch in a clogged granular hopper). To test this hypothesis, we measure the cell nuclear density throughout the experiment. Fig. 3A shows heatmaps of the average nuclear density pre-stimulation and at the end of the experiment, at  $t = 15$  hrs. A pronounced ring of high density around the center, indicates

where cells are likely jammed. Fig. 3B, which shows the average radial projection of the nuclear density, quantifies and emphasizes this problem.

These results emphasize that the continuous local stimulation strategy causes a cellular traffic jam as cells rush towards the wound center and explain the initial accelerated closure rate and subsequent plateau if the stimulation is left on too long. This suggests a hybrid approach to healing which avoids jamming by using a single, 3 hr pulse of local, ring stimulation to boost the initial closure rate, then pauses to allow the system density to relax and naturally heal before jamming can occur. We label this strategy “Single Pulse”. To test this hypothesis, we plot the analogous density heatmaps (Fig. 3C) and density profiles (Fig. 3D), and we show that the single pulse and relaxation strategy does indeed prevent the jamming process by keeping the density profile relatively stable. Moreover, this approach also accelerates healing overall, as shown in the wound dynamics in Fig. 3E and in the  $t = 15$  hrs healing comparison in Fig. 3F. Supplementary Video 8 shows the nuclear density of the Continuous Local Stimulation and the Single Pulse stimulation together, and Supplementary Video 9 shows a representative timelapse of the Single Pulse strategy.

### Designing an optimal pulse sequence for healing

Our single pulse experiments prove that tuning the timescale of stimulation is key to by boosting initial closure rates without inducing long-term jamming, and this raises our next question: is there an optimal strategy to close the wound even faster? Given the large parameter space of pulse sequences (timing, location of ring, etc.) we turn to a minimal, biophysically informed optimal control model (full details in the SI section G) to help refine our control strategy. Briefly, the experimental system is described by a density of active cells that vary in space-time,  $\rho(x, t)$ , and an accompanying velocity field,  $v(x, t)$ , which is subject to control by an external electric field,  $u(x, t)$ . Here we assume the dynamics can be described in 1 space dimension (or in an axisymmetric geometry) for simplicity. Assuming that mass is conserved over the course of an experiment, which we verify using experimental measurements of cell counts, the continuity equation reads

$$\partial_t \rho + \nabla \cdot (\rho v) = 0$$

In a minimal setting of wound healing of an epithelial gash, cells respond to variations in density by moving to close the wound but maintain their integrity. Their motion is resisted by friction with the substrate and with each other, and driven by a combination of density variations and the external electric field, leading to a minimal equation for force balance that reads

$$-\alpha v + v \nabla^2 v - \chi \nabla \rho + u = 0$$

Here  $-\alpha v$  represents friction with the substrate,  $v \nabla^2 v$  represents viscous forces due to mechanical coupling within the sheet,  $-\chi \nabla \rho$  drives motion due to density gradients with a demotactic (Etym., *demos* = population, *taxis* = directed movement) coefficient  $\chi$ , and  $u(x, t)$  is the local control induced by the applied electric stimulus that is as yet unknown.

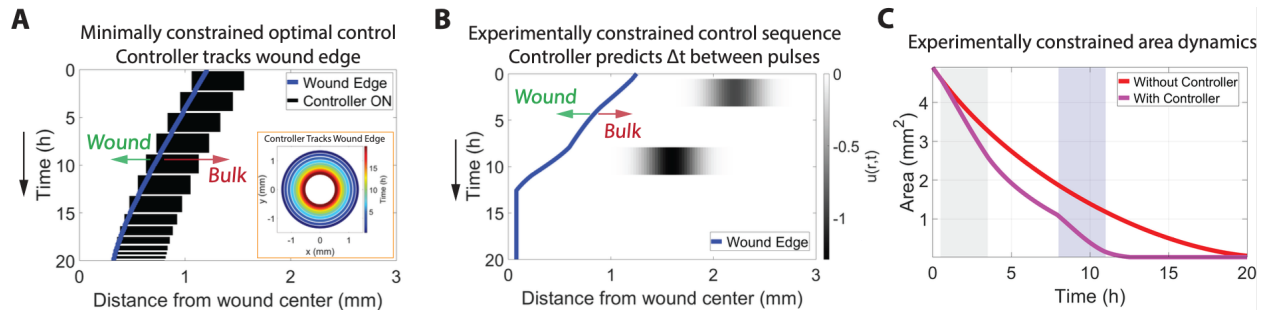


Figure 4. Optimal control solution in the minimally constrained and experimentally constrained limits. (A) Minimally constrained optimal control solution predicts a pulse train that tracks the wound edge in space as it heals in time. The pulses have fixed magnitude,  $u(r, t) = -0.1$ . The wound edge is plotted in blue with two arrows indicating the wounded regions ( $\rho = 0$ ) and bulk regions of finite mass ( $\rho > 0$ ). Inset: temporal color-coded control schematic shows concentric rings which get smaller with time. The outlines show only the center of mass of each pulse for clarity. (B) Experimentally constrained optimal control solution yields a double pulse sequence with pulses offset in space and time with wound boundary plotted in blue. The time delay helps prevent density build-ups which halt healing. (C) Simulated wound area for the experimentally constrained optimal control double pulse sequence (purple) and the naturally healing case (red) without a controller.

To determine this control field, we postulate the control objective as one that minimizes the wound area, *i.e.*, uniformizes the cell density field when starting from a wounded state, subject to an  $L^1$  norm cost of the controller, that physically corresponds to a sparseness cost in space-time (see SI section G), and corresponds to the following formulation of the optimal control problem:

$$\min_{(\rho, v, u)} \mathcal{J}[\rho, u] = \gamma_T A_{open}[\rho(T)] + \int_0^T \left( B[\rho(t)] + \lambda_u \|u(\cdot, t)\|_{L^1_r} \right) dt$$

Where  $\mathcal{J}$  is the cost function composed of a terminal cost ( $\gamma_T A_{open}[\rho(T)]$ ) which penalizes the wound area and a running cost ( $\int_0^T \left( B[\rho(t)] + \lambda_u \|u(\cdot, t)\|_{L^1_r} \right) dt$ ) which penalizes running the controller and minimized subject to the mass and force balance PDE constraints. The normalized epithelial density associated with the wound is modeled by a sharp  $\tanh(x)$  function at the wound boundary. We solved the stochastic optimal control using a recently introduced Adjoint-based approach to solve the Hamilton-Jacobi-Bellman equation, that uses a path integral formulation and continuous-time back-propagation to evaluate the control strategy in terms of the value function<sup>51–55</sup> (see SI section G).

This minimally constrained PDE control problem predicts a pulse-train solution for healing the wound. Shown in Fig. 4A is a kymograph of the solution where the controller dynamically moves the stimulus radius closer to the wound center as the wound heals. The solution provides the first of two critical insights from theory: as the wound naturally changes size while it heals, the optimal controller needs to follow that size change that arises naturally from the biophysical theory subject to the control field.

Tracking the wound edge is a simple and effective strategy, but experimentally validating it requires additional experimental constraints. First, adjusting the stimulus position in space as the wound heals requires changing the device architecture manually. This is challenging, and practically only a single change during an experiment is possible.

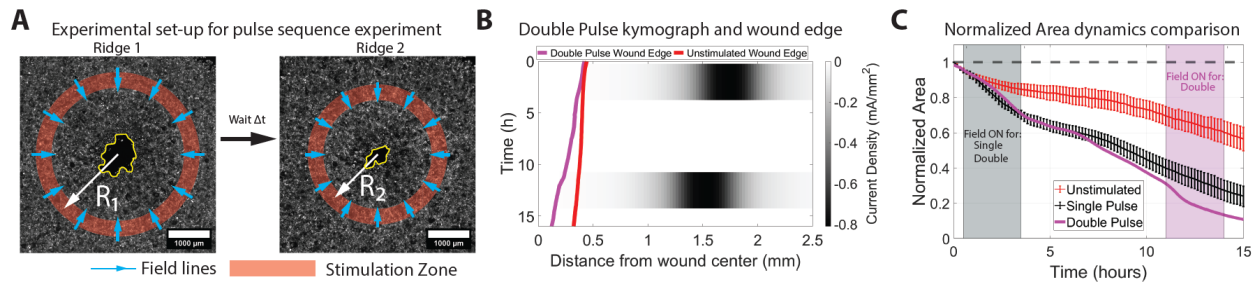


**Figure 5.** Experimental realization of constrained optimal control solution shows better wound healing. (A) Schematic of the double pulse sequence inspired by the predictions of the constrained optimal controller. Two annular ridge devices with radii  $R_1$  and  $R_2$  are overlaid on wounded tissues. Wound boundaries are in yellow. (B) Experimental double pulse control kymograph showing two pulses offset in time and space with the effective wound edge is shown in purple along with the unstimulated wound edge in red for comparison. (C) Normalized area dynamics of the double pulse data compared to the single pulse data with shaded regions for the stimulation pulse periods. After pulse 1, the two traces track one another well. However, pulse 2 accelerates the healing rate again which splits the two traces. The unstimulated case is plotted in red for comparison.

Second, experiments show that placing the annulus too close to the wound edge causes edge retraction (see Fig. S6), so we constrain the minimal distance between the annulus and the wound edge to  $\sim 1$  mm (edge retraction itself is not captured by the model). Finally, we restrict the simulation to 20 hours, a few hours longer than the experimental time to minimize the role of cell division in the process. The cell cycle for the mouse keratinocytes is about 16 hours, and we verified that there were no significant changes in cell counts over this duration. This alters the experimentally constrained optimal control problem (see SI section H for details). Briefly, the cost is subject to the same basic PDE constraints (mass and force balance) but has additional constraints from experiment put in as objectives (see eqn. 8 in SI section H). These constraints help regularize the density and control fields by accounting for mass conservation and spatiotemporal derivatives of the control and velocity fields (see SI section H for details). With these constraints in place, the optimal control problem yields a solution for where to place the two annuli in space and how long to wait between stimulation pulses. In Fig. 4B, we plot the solution to the experimentally constrained optimal control problem with the wound edge shown in red. Accompanying movies of the wound density and controller for the experimentally constrained case are shown in Supplementary Video 10. Here, we observe that the controller predicts two, 3 hour stimulation pulses at  $R_1 \approx 1.1$  mm and  $R_2 \approx 0.75$  mm separated in time by  $\Delta t = 6$  hours where the second pulse is stronger in magnitude. Fig. 4C shows the area of the electrically stimulated wound compared to the case in the absence of an electric field, demonstrating the speed-up of  $\sim 40\%$  for wound-closure.

We took inspiration from these predictions and test them experimentally using our final control strategy that we call “Double Pulse”. To clearly demonstrate this schema, we show a schematic set-up in Fig. 5A, where two annular ridges of radii  $R_1 = 1.75$  mm and  $R_2 = 1.5$  mm representing the two pulses overlay a tissue micrograph. Between the two pulses there is a time delay of  $\Delta t = 7$  hrs; this controller strategy is captured in the kymograph in Fig. 5B, which also shows the wound boundary compared to that of the unstimulated control. Supplementary Video 11 shows the Double Pulse experiment.

As before, we evaluate the controller performance by plotting the healing dynamics in Fig. 5C. We include the results from the Single Pulse experiments as a point of comparison and the unstimulated wound as the baseline. We see two regions (corresponding to the two pulses) where healing is accelerated via the optimal control generated stimulation pulses. The Double Pulse strategy far outperforms all other strategies. Videos of various alternative instantiations of Double Pulse sequences can be found in Supplementary Videos 12 and 13, both of which underperform the optimal solution.

## **Discussion:**

Using our new device architecture which can produce local electric fields, we showed that narrow localized electric stimulation can induce orientational alignment of tissue motion over a much broader length scale via mechanical coupling. This insight served as the guiding principle for accelerating healing in a 2D wound model. By subjecting wounds to a local annular ring field placed about one millimeter from the wound edge, we were able to improve initial healing rates while avoiding tissue damage. When the local command is left on, however, cells within the tissue jam, and this increased density slows overall healing. To address this issue, we used a single stimulation pulse which boosts initial closure rates and allows the system density to equilibrate. Finally, we used a simple physics-informed optimal control model to further enhance healing. The optimal control model predicted that pulsed fields which track the wound edge in space and offset in time would improve healing rates, and we validated this with experiment.

These findings highlight two principles. First, local perturbations are often exceptionally efficient by construction and necessary in application. In nature, a sheepdog can control a herd by applying local pressure to its boundary without interacting with the bulk. Our set-up allows for local stimulation within a tissue, and mechanical coupling extends its effects spatially. However, local stimulation only works when well-positioned in space and time. Global or poorly placed stimulation patterns did not accelerate healing, and in many instances led to tissue damage. Second, control approaches which work with the mechanics of a collective have the potential for more effective control while minimizing system damage (death, in the case of tissues). Here, we focused on collective wound healing in mouse skin epithelia. In this problem context, there are myriad avenues for improvement and follow-up studies including closed-loop control using real-time readouts of densities and velocities, individually addressable microelectrode arrays for more precise control over stimulation structures, and refinements of the model which include viscoelasticity or even a physics-agnostic approach which uses microscopy data alone. Each of these will be an important step towards accelerated wound healing devices in the future. However, we stress that all living crowd systems share core similarities, and our analyses and control strategies may generalize to other systems, such as human crowds, where respecting the natural collective principles of a system can improve our ability to control them.

## **Acknowledgements**

This work was supported in part by Eric and Wendy Schmidt Transformative Technology Fund, NIH Award R35 GM133574-07, and NSF CAREER Award 2412942. J.S.Y. is supported by the Ommen Darling postdoctoral fellowship.

## **Declaration of Interests**

D.J.C., J.S.Y., and Y.L. have filed patent applications based on the method developed in this work.

## **Data and code availability**

Key microscopy data and data to generate figures from the main text will be available on Zenodo. The code for the optimal control analysis will be accessible through GitHub.

## References

1. Park, S., Gonzalez, D.G., Guirao, B., Boucher, J.D., Cockburn, K., Marsh, E.D., Mesa, K.R., Brown, S., Rompolas, P., Haberman, A.M., et al. (2017). Tissue-scale coordination of cellular behaviour promotes epidermal wound repair in live mice. *Nat Cell Biol* *19*, 155–163. <https://doi.org/10.1038/ncb3472>.
2. Eming, S.A., Martin, P., and Tomic-Canic, M. (2014). Wound repair and regeneration: Mechanisms, signaling, and translation. *Sci. Transl. Med.* *6*. <https://doi.org/10.1126/scitranslmed.3009337>.
3. Gurtner, G.C., Werner, S., Barrandon, Y., and Longaker, M.T. (2008). Wound repair and regeneration. *Nature* *453*, 314–321. <https://doi.org/10.1038/nature07039>.
4. Bialek, W., Cavagna, A., Giardina, I., Mora, T., Silvestri, E., Viale, M., and Walczak, A.M. (2012). Statistical mechanics for natural flocks of birds. *Proc. Natl. Acad. Sci. U.S.A.* *109*, 4786–4791. <https://doi.org/10.1073/pnas.1118633109>.
5. Ballerini, M., Cabibbo, N., Candelier, R., Cavagna, A., Cisbani, E., Giardina, I., Lecomte, V., Orlandi, A., Parisi, G., Procaccini, A., et al. (2008). Interaction ruling animal collective behavior depends on topological rather than metric distance: Evidence from a field study. *Proc. Natl. Acad. Sci. U.S.A.* *105*, 1232–1237. <https://doi.org/10.1073/pnas.0711437105>.
6. Cavagna, A., Cimarelli, A., Giardina, I., Parisi, G., Santagati, R., Stefanini, F., and Viale, M. (2010). Scale-free correlations in starling flocks. *Proc. Natl. Acad. Sci. U.S.A.* *107*, 11865–11870. <https://doi.org/10.1073/pnas.1005766107>.
7. Azaïs, M., Blanco, S., Bon, R., Fournier, R., Pillot, M.-H., and Gautrais, J. (2018). Traveling pulse emerges from coupled intermittent walks: A case study in sheep. *PLoS ONE* *13*, e0206817. <https://doi.org/10.1371/journal.pone.0206817>.
8. Ginelli, F., Peruani, F., Pillot, M.-H., Chaté, H., Theraulaz, G., and Bon, R. (2015). Intermittent collective dynamics emerge from conflicting imperatives in sheep herds. *Proc. Natl. Acad. Sci. U.S.A.* *112*, 12729–12734. <https://doi.org/10.1073/pnas.1503749112>.
9. Gómez-Nava, L., Bon, R., and Peruani, F. (2022). Intermittent collective motion in sheep results from alternating the role of leader and follower. *Nat. Phys.* *18*, 1494–1501. <https://doi.org/10.1038/s41567-022-01769-8>.
10. Silverberg, J.L., Bierbaum, M., Sethna, J.P., and Cohen, I. (2013). Collective Motion of Humans in Mosh and Circle Pits at Heavy Metal Concerts. *Phys. Rev. Lett.* *110*, 228701. <https://doi.org/10.1103/PhysRevLett.110.228701>.
11. Bain, N., and Bartolo, D. (2019). Dynamic response and hydrodynamics of polarized crowds. *Science* *363*, 46–49. <https://doi.org/10.1126/science.aat9891>.
12. Gu, F., Guiselin, B., Bain, N., Zuriguel, I., and Bartolo, D. (2025). Emergence of collective oscillations in massive human crowds. *Nature* *638*, 112–119. <https://doi.org/10.1038/s41586-024-08514-6>.

13. Gosain, A., and DiPietro, L.A. (2004). Aging and Wound Healing. *World j. surg.* *28*, 321–326. <https://doi.org/10.1007/s00268-003-7397-6>.
14. Gould, L., Abadir, P., Brem, H., Carter, M., Conner-Kerr, T., Davidson, J., DiPietro, L., Falanga, V., Fife, C., Gardner, S., et al. (2015). Chronic wound repair and healing in older adults: Current status and future research. *Wound Repair Regeneration* *23*, 1–13. <https://doi.org/10.1111/wrr.12245>.
15. Nzigou Mombo, B., Bijonowski, B.M., Raab, C.A., Niland, S., Brockhaus, K., Müller, M., Eble, J.A., and Wegner, S.V. (2023). Reversible photoregulation of cell-cell adhesions with opto-E-cadherin. *Nat Commun* *14*, 6292. <https://doi.org/10.1038/s41467-023-41932-0>.
16. Wang, X., He, L., Wu, Y.I., Hahn, K.M., and Montell, D.J. (2010). Light-mediated activation reveals a key role for Rac in collective guidance of cell movement in vivo. *Nat Cell Biol* *12*, 591–597. <https://doi.org/10.1038/ncb2061>.
17. Valon, L., Marín-Llauradó, A., Wyatt, T., Charras, G., and Trepats, X. (2017). Optogenetic control of cellular forces and mechanotransduction. *Nat Commun* *8*, 14396. <https://doi.org/10.1038/ncomms14396>.
18. Keenan, T.M., and Folch, A. (2008). Biomolecular gradients in cell culture systems. *Lab Chip* *8*, 34–57. <https://doi.org/10.1039/B711887B>.
19. Berthier, E., and Beebe, D.J. (2014). Gradient generation platforms: new directions for an established microfluidic technology. *Lab Chip* *14*, 3241–3247. <https://doi.org/10.1039/C4LC00448E>.
20. Shim, G., Devenport, D., and Cohen, D.J. (2021). Overriding native cell coordination enhances external programming of collective cell migration. *Proc. Natl. Acad. Sci. U.S.A.* *118*, e2101352118. <https://doi.org/10.1073/pnas.2101352118>.
21. Copos, C., Sun, Y.-H., Zhu, K., Zhang, Y., Reid, B., Draper, B., Lin, F., Yue, H., Bernadskaya, Y., Zhao, M., et al. (2024). Galvanotactic directionality of cell groups depends on group size. Preprint at *Cell Biology*, <https://doi.org/10.1101/2024.08.13.607794> <https://doi.org/10.1101/2024.08.13.607794>.
22. Cohen, D.J., James Nelson, W., and Maharbiz, M.M. (2014). Galvanotactic control of collective cell migration in epithelial monolayers. *Nature Mater* *13*, 409–417. <https://doi.org/10.1038/nmat3891>.
23. Wolf, A.E., Heinrich, M.A., Breinyn, I.B., Zajdel, T.J., and Cohen, D.J. (2022). Short-term bioelectric stimulation of collective cell migration in tissues reprograms long-term supracellular dynamics. *PNAS Nexus* *1*, pgac002. <https://doi.org/10.1093/pnasnexus/pgac002>.
24. Cho, Y., Son, M., Jeong, H., and Shin, J.H. (2018). Electric field–induced migration and intercellular stress alignment in a collective epithelial monolayer. *MBoC* *29*, 2292–2302. <https://doi.org/10.1091/mbc.E18-01-0077>.
25. Lin, Y., Yodh, J.S., Rodriguez, C., Kreymborg, P., and Cohen, D.J. SCHEPHERD: A universal platform for high-throughput, high-resolution, and programmable control of cell behavior through bioelectric stimulation.

26. Allen, G.M., Mogilner, A., and Theriot, J.A. (2013). Electrophoresis of Cellular Membrane Components Creates the Directional Cue Guiding Keratocyte Galvanotaxis. *Current Biology* 23, 560–568.
27. Zhao, M., Song, B., Pu, J., Wada, T., Reid, B., Tai, G., Wang, F., Guo, A., Walczysko, P., Gu, Y., et al. (2006). Electrical signals control wound healing through phosphatidylinositol-3-OH kinase- $\gamma$  and PTEN. *Nature* 442, 457–460. <https://doi.org/10.1038/nature04925>.
28. Shim, G., Breinyn, I.B., Martínez-Calvo, A., Rao, S., and Cohen, D.J. (2024). Bioelectric stimulation controls tissue shape and size. *Nat Commun* 15, 2938. <https://doi.org/10.1038/s41467-024-47079-w>.
29. Lyon, J.G., Carroll, S.L., Mokarram, N., and Bellamkonda, R.V. (2019). Electrotaxis of Glioblastoma and Medulloblastoma Spheroidal Aggregates. *Sci Rep* 9, 5309. <https://doi.org/10.1038/s41598-019-41505-6>.
30. Belliveau, N.M., Footer, M.J., Platenkamp, A., Rodriguez, C., Kim, H., Prinz, C.K., van Loon, A.P., Lin, Y., Eustis, T.E., Chan, M.M., et al. Galvanin (TMEM154) is an electric-field sensor for directed cell migration.
31. Saw, T.B., Gao, X., Li, M., He, J., Le, A.P., Marsh, S., Lin, K., Ludwig, A., Prost, J., and Lim, C.T. (2022). Transepithelial potential difference governs epithelial homeostasis by electromechanics. *Nat. Phys.* 18, 1122–1128. <https://doi.org/10.1038/s41567-022-01657-1>.
32. Barker, A.T., Jaffe, L.F., and Venable, J.W. (1982). The glabrous epidermis of cavies contains a powerful battery. *American Journal of Physiology-Regulatory, Integrative and Comparative Physiology* 242, R358–R366. <https://doi.org/10.1152/ajpregu.1982.242.3.R358>.
33. Kennard, A.S., and Theriot, J.A. (2020). Osmolarity-independent electrical cues guide rapid response to injury in zebrafish epidermis. *eLife* 9, e62386. <https://doi.org/10.7554/eLife.62386>.
34. Nuccitelli, R. (2003). A Role for Endogenous Electric Fields in Wound Healing. In *Current Topics in Developmental Biology* (Elsevier), pp. 1–26. [https://doi.org/10.1016/S0070-2153\(03\)58001-2](https://doi.org/10.1016/S0070-2153(03)58001-2).
35. Zhao, M. (2009). Electrical fields in wound healing—An overriding signal that directs cell migration. *Seminars in Cell & Developmental Biology* 20, 674–682. <https://doi.org/10.1016/j.semcdb.2008.12.009>.
36. McCaig, C.D., Rajnicek, A.M., Song, B., and Zhao, M. (2005). Controlling Cell Behavior Electrically: Current Views and Future Potential. *Physiological Reviews* 85, 943–978. <https://doi.org/10.1152/physrev.00020.2004>.
37. Reid, B., Song, B., McCaig, C.D., and Zhao, M. (2005). Wound healing in rat cornea: the role of electric currents. *The FASEB Journal* 19, 379–386. <https://doi.org/10.1096/fj.04-2325com>.
38. Ma, L., Reid, B., Baird, L., Calderón-Colón, X., Ryzhuk, V., Kim, S., Sandoval-Castellanos, A.M., Murphy, C.J., Hamilton, L.H., Trexler, M.M., et al. (2026). EMERGE patch, a novel electrogenic engineered material to enhance healing of severe corneal wounds. *Biomaterials* 326, 123689. <https://doi.org/10.1016/j.biomaterials.2025.123689>.

39. Song, J.W., Ryu, H., Bai, W., Xie, Z., Vázquez-Guardado, A., Nandoliya, K., Avila, R., Lee, G., Song, Z., Kim, J., et al. (2023). Bioresorbable, wireless, and battery-free system for electrotherapy and impedance sensing at wound sites. *Science Advances* 9, eade4687. <https://doi.org/10.1126/sciadv.ade4687>.
40. Jiang, Y., Trotsyuk, A.A., Niu, S., Henn, D., Chen, K., Shih, C.-C., Larson, M.R., Mermin-Bunnell, A.M., Mittal, S., Lai, J.-C., et al. (2023). Wireless, closed-loop, smart bandage with integrated sensors and stimulators for advanced wound care and accelerated healing. *Nat Biotechnol* 41, 652–662. <https://doi.org/10.1038/s41587-022-01528-3>.
41. Couzin, I.D., Krause, J., Franks, N.R., and Levin, S.A. (2005). Effective leadership and decision-making in animal groups on the move. *Nature* 433, 513–516. <https://doi.org/10.1038/nature03236>.
42. Reebs, S.G. (2000). Can a minority of informed leaders determine the foraging movements of a fish shoal? *Animal Behaviour* 59, 403–409. <https://doi.org/10.1006/anbe.1999.1314>.
43. Sankey, D.W.E., Storms, R.F., Musters, R.J., Russell, T.W., Hemelrijk, C.K., and Portugal, S.J. (2021). Absence of “selfish herd” dynamics in bird flocks under threat. *Current Biology* 31, 3192-3198.e7. <https://doi.org/10.1016/j.cub.2021.05.009>.
44. Couzin, I.D., Krause, J., James, R., Ruxton, G.D., and Franks, N.R. (2002). Collective Memory and Spatial Sorting in Animal Groups. *Journal of Theoretical Biology* 218, 1–11. <https://doi.org/10.1006/jtbi.2002.3065>.
45. Early, J., Aalders, J., Arnott, E., Wade, C., and McGreevy, P. (2020). Sequential Analysis of Livestock Herding Dog and Sheep Interactions. *Animals* 10, 352. <https://doi.org/10.3390/ani10020352>.
46. Strömbom, D., Mann, R.P., Wilson, A.M., Hailes, S., Morton, A.J., Sumpter, D.J.T., and King, A.J. (2014). Solving the shepherding problem: heuristics for herding autonomous, interacting agents. *J. R. Soc. Interface*. 11, 20140719. <https://doi.org/10.1098/rsif.2014.0719>.
47. Ranganathan, A., Guo, D., Heyde, A., Gupta, A., and Mahadevan, L. (2024). Emergent Strategies for Shepherding a Flock. Preprint at arXiv, <https://doi.org/10.48550/arXiv.2211.04352> <https://doi.org/10.48550/arXiv.2211.04352>.
48. O’Keefe, E.J., Briggaman, R.A., and Herman, B. (1987). Calcium-induced assembly of adherens junctions in keratinocytes. *The Journal of cell biology* 105, 807–817. <https://doi.org/10.1083/jcb.105.2.807>.
49. Rüksam, M., Broussard, J.A., Wickström, S.A., Nekrasova, O., Green, K.J., and Niessen, C.M. (2018). Adherens Junctions and Desmosomes Coordinate Mechanics and Signaling to Orchestrate Tissue Morphogenesis and Function: An Evolutionary Perspective. *Cold Spring Harb Perspect Biol* 10, a029207. <https://doi.org/10.1101/cshperspect.a029207>.
50. Thielicke, W., and Sonntag, R. (2021). Particle Image Velocimetry for MATLAB: Accuracy and enhanced algorithms in PIVlab. *JORS* 9, 12. <https://doi.org/10.5334/jors.334>.
51. Bellman, R. (2010). *Dynamic programming First Princeton landmarks in mathematics edition*. (Princeton University Press).

52. Krishnan, V., Sinha, S., and Mahadevan, L. (2024). Hamiltonian bridge: A physics-driven generative framework for targeted pattern control. Preprint at arXiv, <https://doi.org/10.48550/arXiv.2410.12665> <https://doi.org/10.48550/arXiv.2410.12665>.
53. Sinha, S., Krishnan, V., and Mahadevan, L. (2023). Optimal control of interacting active particles on complex landscapes. Preprint at arXiv, <https://doi.org/10.48550/arXiv.2311.17039> <https://doi.org/10.48550/arXiv.2311.17039>.
54. Pontrjagin, L.S. ed. (1964). The mathematical theory of optimal processes Reprint. (MacMillan).
55. Bryson, A.E. (2018). Applied optimal control: optimization, estimation, and control (CRC Press LLC).